

Overcoming limitations in water-ethanol sprayed superstrate solar cells by compositional engineering of $\text{Cu}_2\text{CdSn}(\text{S},\text{Se})_4$

David Payno Zarceño ^{a,*}, Maxim Guc ^a, Samrana Kazim ^{b,c}, Alejandro Pérez-Rodríguez ^{a,d},
Shahzada Ahmad ^{b,c,*}

^a Catalonia Energy Research Institute (IREC), 08930, Barcelona, Spain

Email: dpayno@irec.cat

^b BCMaterials, Basque Center for Materials, Applications, and Nanostructures, Bld. Martina Casiano, UPV/EHU Science Park, Barrio Sarriena s/n, 48940 Leioa, Spain

Email: shahzada.ahmad@bcmaterials.net

^c IKERBASQUE, Basque Foundation for Science, 48009 Bilbao, Spain

^d IN2UB, Departament d'Enginyeria Electrònica i Biomèdica, Universitat de Barcelona, 08028 Barcelona, Spain

Abstract

The increasing demand for solar energy requires materials from earth-abundant elements to ensure cost-effective production. One such light harvester $\text{Cu}_2\text{CdSn}(\text{S},\text{Se})_4$ fulfills this property. We report the development of functional solar cells based on $\text{Cu}_2\text{CdSn}(\text{S},\text{Se})_4$ which is hereto unreported. Furthermore, we deposited the thin films of $\text{Cu}_2\text{CdSn}(\text{S},\text{Se})_4$ by spray pyrolysis using environmentally benign solvents, in a superstrate architecture, reducing the potential cost of up-scaling, and enabling its use in semi-transparent or tandem solar cells and specifically the environmental hazards. We analyze the $\text{Cu}_2\text{CdSn}(\text{S},\text{Se})_4$ and their optoelectronic characteristics with different sulfur and selenium ratio in the composition. We noted that Se is homogeneously distributed in the absorber and electron transport layer, forming a $\text{Cd}(\text{S},\text{Se})$ phase that impacts the optoelectronic properties. The introduction of Se, <30 %, is found to have a positive impact on the solar cell performance, largely improving the fill factor and absorption in the infrared region, while the voltage deficit is reduced. The device with a $\text{Cu}_2\text{CdSn}(\text{S}_{2.8}\text{Se}_{1.2})$ composition, measured a 3.5% solar-to-electric conversion efficiency, which is on par with the values for chalcogenides reported, and the first report using $\text{Cu}_2\text{CdSn}(\text{S},\text{Se})_4$. We identified the critical factors that limit the efficiency, revealing pathways to further reduce the losses and improve the performance. This work provides the first proof of concept of a novel material, paving the way for developing cost-efficient solar cells based on earth-abundant materials.

Keywords: Thin film, photovoltaic, solar cell, spray pyrolysis, superstrate architecture, chalcogenides, $\text{Cu}_2\text{CdSn}(\text{S},\text{Se})_4$

1. Introduction

The current opportunities in the photovoltaic (PV) sector are constrained, mainly due to the requirements of optoelectronic properties and the quality of materials. A suitable bandgap, high conductivity, large charge diffusion length, slow bulk and interface charge recombination, and rational band alignment of the electron and hole transport layers are some of the key prerequisites that demand considerable scientific effort during the optimization of materials to yield high efficiency.¹ Moreover, the developed materials should compete with the existing PV technologies in terms of efficiency, durability, versatility, low-cost manufacturing processes, and avoid the use of scarce or critical raw elements. Thus, finding new light harvester materials is challenging, but of high importance. Since each light harvester possesses a unique set of properties that are suited for a particular need or specific application, such as the absorption of a specific range of wavelengths, semi-transparency, or flexibility.

Among the emerging materials, inorganic chalcogenides composed of earth-abundant elements, such as $\text{Cu}_2\text{ZnSnS}_4$ (CZTS), have drawn attention for their potential to develop cost-efficient thin film technologies free of scarce elements. Chemical routes for the preparation of inorganic chalcogenides have demonstrated that high-quality films can be obtained with simple and cost-effective methods. The maximum efficiencies in this class of solar cells have been obtained by spin coating,^{2,3} while other scalable methods such as ink-jet printing⁴, spray coating⁵, or spray pyrolysis⁶ also demonstrated high efficiencies. Spray pyrolysis is particularly interesting due to its simplicity, high throughput, and low material usage, while benign solvents such as water and ethanol or its binary solvents result in homogeneous films.⁷⁻⁹

The intrinsic problems that limit the efficiency and thus large-scale implementation of CZTS have been extensively studied in the last decade, and yet the efficiency of this technology has remained stable. In particular, recombination centers due to the Cu – Zn disorder and defects¹⁰⁻¹² low electron diffusion length,¹³ and large band tailing^{14,15} are among the constraints that induce high voltage deficit and limit efficiency.¹⁶ Kesterite based-solar cells are being developed using similar substrate architecture, as of CIGS, despite having a problematic interface with both the Mo/Mo(S,Se) back contact and the CdS front contact, requiring complex strategies to mitigate the interface recombination.¹⁷⁻²⁰ On the other hand, the use of kesterite in a superstrate architecture has not been widely studied and is rapidly evolving as an alternative to improve the interfaces while reducing the processing cost of solar cells. In a superstrate architecture, a wide variety of materials such as hole transport layer (HTL) and back contact can be probed, which can facilitate the carrier collection at the back surface, and can be adapted to semi-transparent, bifacial, or tandem solar cells. However, typical electron selective layers (ETL), such as CdS, have low compatibility with CZTS in a superstrate architecture.²¹ Here, a compact or

nanostructured thin film of TiO_2 can be adopted as ETL.²² TiO_2 can act as a stable and protective layer for the FTO while also reducing the risk of shunt paths. However, the growth of CZTS on TiO_2 is challenging, thus a CdS interlayer is usually necessary, making it hard to control the composition of both the absorber and CdS due to a Cd – Zn exchange during the annealing.^{23,24}

The intrinsic limitations of CZTS can be overcome by doping and alloying composition, to tune its properties. The diffusion of alkali elements such as Na and Li has a positive impact on grain boundary passivation,^{25–28} while isovalent elements can be incorporated into the absorber or the interface to mitigate defects and reduce the recombination, such as Ag for Cu, Cd and Ba for Zn, or Ge for Sn. The recent record efficiency in CZTS implements such elements into their composition. This approach is also useful to adapt the CZTS in a superstrate architecture,^{9,29} opening a window of applications for the fabricated solar cells. The substitution of Zn by Cd into the bulk of the absorber layer was an effective method to improve the crystal structural ordering,^{30,31} reducing the band tailings and increasing the photoluminescence, while its implementation in the surface largely improves the junction quality with CdS, yielding the best results on CZTS. Higher than 10 % efficiency has been reported in a solar cell with a $\text{Cu}_2\text{CdSnS}_4$ composition recently,³² which demonstrates its potential.

Subsequently, the introduction of different chalcogens in the composition is adopted in kesterite-based solar cells to obtain $\text{Cu}_2\text{ZnSn}(\text{S},\text{Se})_4$ (CZTSSe) solid solutions.³³ Selenium-rich compositions possess a lower band gap and produce homogeneous films with larger grains and lower secondary phases, improving the carrier lifetime and thus lowering the voltage deficit and improving the fill factor (FF).^{34–36} The materials based on $\text{Cu}_2\text{CdSnSe}_4$ possess a band gap of 0.96 eV and show p-type conductivity.³⁷ With a Cu-rich composition, this has also drawn attention for thermoelectricity application.^{38–40} A preliminary work of using $\text{Cu}_2\text{CdSn}(\text{S},\text{Se})_4$ (CCTSSe) as a light absorber layer in a substrate architecture the fabricated device measured an efficiency of 3.1 %⁴¹ suggesting its potential in photovoltaics. Due to its resemblances to CZTSSe, an increase in Se content in the CCTSSe absorber can further improve the optoelectronic properties, while the band gap can be tuned with the sulfur-to-selenium ratio. Avoiding the use of Zn in the composition, also increase the compatibility of this absorber with a superstrate structure, since the Cd – Zn exchange problem is avoided.

On the other hand, the use of Cd in PV can be interesting as the Cd by-product generated in the Zn mining,⁴² can find applications, and Cd chalcogenides are the safest and most stable form of Cd. These reasons place CCTSSe as a desirable material for the development of a large-scale, stable, and low-cost PV technology.

Here, we report the first proof of concept of functional superstrate CCTSSe solar cells, using spray pyrolysis from a simple molecular solution with benign solvents for the preparation of the

absorber film. We study the effects of adding Se in the annealing step. The prepared devices show an improved FF and a broader EQE in both short and long wavelengths, measuring a maximum power conversion efficiency (PCE) of up to 3.5 % with a 30 % of Se to S relative content. The band gap of the absorber can be tuned, from 1.4 eV to lower values depending on the Se content. Our results suggest that Se addition increases the diffusion length of the carriers and reduces the resistance, reaching suitable properties for efficient superstrate solar cells.

2. Experimental

Solar cells fabrication

Solar cells were prepared with the superstrate architecture, starting with a clean substrate of commercial FTO-coated glass, a compact TiO_2 was deposited by spray pyrolysis at 500 °C, using a solution of **g** titanium(IV) diisopropoxide bis(acetylacetonate) (Merck) diluted in absolute ethanol with a ratio of 1:19. Mesoporous TiO_2 , was deposited by spin coating at 2000 rpm a solution of TiO_2 paste (18NR-T, Greatcell) dispersed in ethanol, with a concentration of 125 mg/ml, followed by an anneal at 500 °C on a hotplate. CdS film was deposited by chemical bath deposition, by introducing the samples in a 370 mL aqueous solution containing 75 mg of $\text{Cd}(\text{SO}_4)_2$, 200 mg of thiourea, and 18.2 mL of ammonia solution (30 %) at 65 °C for 10 minutes.

The precursor film of $\text{Cu}_2\text{CdSnS}_4$ was deposited on top by spray pyrolysis. The salt precursors CuCl_2 , $\text{Cd}(\text{NO}_3)_2$, and SnCl_2 were separately dissolved in ethanol with a 0.1 M concentration, while thiourea was dissolved in water with a 1 M concentration. The sprayed solution was prepared by mixing the CuCl_2 , $\text{Cd}(\text{NO}_3)_2$, SnCl_2 , and thiourea solutions, following the procedure,⁹ achieving a water and ethanol mix with a 1:1 ratio. The prepared solution was sprayed on the pre-heated substrates at 340 °C. A sulfurization or sulfo-selenization treatment at 530 °C for 1 hour was applied to the stack inside a closed tubular furnace, in an argon atmosphere. Varying amounts of sulfur and selenium powder were placed inside the furnace, to obtain compositions of $\text{Cu}_2\text{CdSn}(\text{S},\text{Se})_4$ with different sulfur and selenium ratios, as summarized in **We** noted that a further increase of Se content did not result in the devices with reliable efficiency, due to limitations in annealing conditions. Optimization of the annealing conditions will be necessary to reach reliable CCTSSe compositions with higher Se content.

Table 1.

Following the characterization of the materials, the PV devices were fabricated with a conductive graphite paste (GST 4500), followed by another highly conductive paste of Ag (RS PRO), both deposited by doctor-blade, with a total thickness of ~ 0.2 mm. Graphite possesses a deep work function of 5 eV that provides an efficient hole extraction while maintaining a low

cost for both the materials and the deposition method. A vinyl mask was used to define the active area, with a diameter of 0.053 cm^2 by microscope imaging. Finally, all the samples were heated at $100\text{ }^{\circ}\text{C}$ for 10 minutes on a hotplate in the air to improve the graphite and Ag conductivity.

Characterizations

Energy Dispersive X-ray spectroscopy (EDX) was performed with a Quantax75 equipped with a TM4000 Series scanning electron microscope (SEM). SEM images were recorded with a Hitachi S-3400 electron microscope at 5 kV of acceleration potential. X-ray diffractograms (XRD) were measured on the final device, without the graphite back contact, with a Cubix3 system from PANalytical with a Cu anode. Raman spectra were measured using FHR 640 (Horiba) monochromator coupled to a deep-cooled CCD detector. The measurements were performed in the backscattering configuration and a solid-state laser (532 nm , $\sim 20\text{ W/cm}^2$) was used as an excitation source. The spectral position was calibrated by imposing the main Raman peak of monocrystalline Si to 520 cm^{-1} . The measurements were made in several points (up to 20) for each sample to define the lateral homogeneity of the sample. Transmittance spectra were recorded with an Agilent Cary 60 UV–Vis spectrometer.

The devices were characterized by external quantum efficiency (EQE) measurements on a PVE300 Bentham system, consisting of a 150 W Xenon lamp and a 1/4m monochromator, in a range from 300 – 1200 nm in steps of 5 nm, and calibrated with Si and Ge reference photodiodes. Current density-voltage (J – V) curves were measured using a Keithley 2400 source meter and a Sun 3000 AAA class solar simulator from Abet Technology under AM 1.5G irradiance. The C – V measurements were performed with a Keysight E4990A impedance analyzer and a homemade faraday cage four-probe setup. Samples were kept in dark conditions during the measurement. The selected frequency for data analysis was 100 kHz, with a 20 mV AC perturbation. The measurements were performed in a voltage range between -1 and +1 V.

3. Results and Discussion

3.1 Characterization of the materials and layers

To obtain $\text{Cu}_2\text{CdSn}(\text{S}_{4-y}\text{Se}_y)$ with compositions of different S to Se ratios, the as-deposited precursor layers were submitted to a sulfo-selenization treatment at $530\text{ }^{\circ}\text{C}$, by adding different amounts of selenium and sulfur powders into a semi-close quartz ampoule, inside the tubular furnace. The resulting layer composition is shown in **We** noted that a further increase of Se content did not result in the devices with reliable efficiency, due to limitations in annealing

conditions. Optimization of the annealing conditions will be necessary to reach reliable CCTS_{Se} compositions with higher Se content.

Table 1. The ratio of selenium to sulfur changes to 0.15 and 0.3 for the samples annealed with 25 mg and 50 mg of selenium respectively. To label the samples, the value of $y=4(\text{Se}/\text{S}+\text{Se})$ is used. Conversely to thermoelectric applications, a Cu-poor and Cd-rich composition was maintained to reduce CuS_x secondary phases and promote V_{Cu} defects which provide p-type doping.⁴³ We noted that a further increase of Se content did not result in the devices with reliable efficiency, due to limitations in annealing conditions. Optimization of the annealing conditions will be necessary to reach reliable CCTS_{Se} compositions with higher Se content.

Table 1. Post-deposition treatment conditions and compositional ratios of $\text{Cu}_2\text{CdSn}(\text{S}_{4-y}\text{Se}_y)$ thin films.

Sample (y)	S powder (mg)	Se powder (mg)	Composition	Measured ratio (EDX)		
				Se/(S+Se)	Cu/(Cd+Sn)	Cd/Sn
0	100	0	$\text{Cu}_2\text{CdSnS}_4$	0	0.82	1.23
0.6	75	25	$\text{Cu}_2\text{CdSn}(\text{S}_{3.4}\text{Se}_{0.6})$	0.15	0.86	1.20
1.2	50	50	$\text{Cu}_2\text{CdSn}(\text{S}_{2.8}\text{Se}_{1.2})$	0.3	0.76	1.09

The microstructure of the thin film with different compositions was deduced, (

Figure 1), revealing a compact layer of grains with sizes in the order of 100 nm. The thin film with Se shows voids and pinholes between the grains, with some areas of the surface covered with fine grains. The appearance of these fine grains suggests that an individual optimization of the annealing treatment is necessary for each composition to achieve higher-quality films. Temperatures as high as 590 °C can further increase the crystallinity of CCTS,^{44,45} however, these temperatures may degrade the FTO and underlayers used.

In SEM cross-section images, the layers can be distinguished. The region marked with blue corresponds to the FTO, with a thickness of ~550 nm. In the region marked with yellow, the mesoporous TiO_2 and CdS layers are mixed, comprising a thickness of ~150 nm. The thickness of the absorber layer, marked in red, is estimated to be ~450 nm on average.

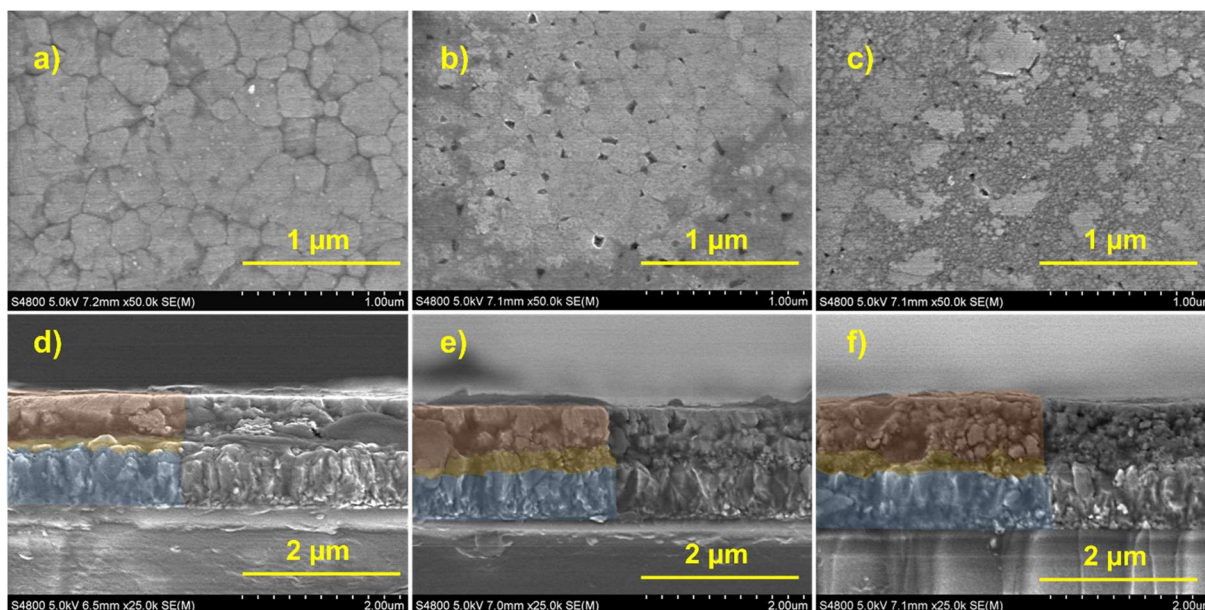


Figure 1. SEM top and cross-sectional view of samples prepared with a composition of a), d) $y=0$, b), e) $y=0.6$, c), f) $y=1.2$, respectively, where the distinctive regions corresponding to different layers are marked.

XRD studies were carried out to identify the predominant phases present in the thin films (**Figure 2**). Three phases can be distinguished, corresponding to the FTO, the ETL, and the light absorber. The peaks from FTO can be deduced in all the patterns, suggesting the material is resistant to the high-temperature treatments and is not affected by the chalcogen atmosphere. Conversely, the peaks corresponding to the absorber material and the ETL are shifted to a lower 2θ value with the presence of selenium in the composition, revealing that Se is forming $\text{Cd}(\text{S},\text{Se})$ (detailed in **Figure S1a**). The lattice parameter values are calculated in **Table 2** for the $\text{Cd}(\text{S},\text{Se})$ and the CCTSSe layers, suggesting an increase in cell size in both cases, since selenium atoms are bigger than sulfur atoms. These results suggest that sulfur and selenium are homogeneously distributed, forming an ETL with a composition close to $\text{Cd}(\text{S}_{0.75}\text{Se}_{0.15})$ for the sample $y = 0.6$, and a $\text{Cd}(\text{S}_{0.6}\text{Se}_{0.3})$ in the $y = 1.2$ sample.

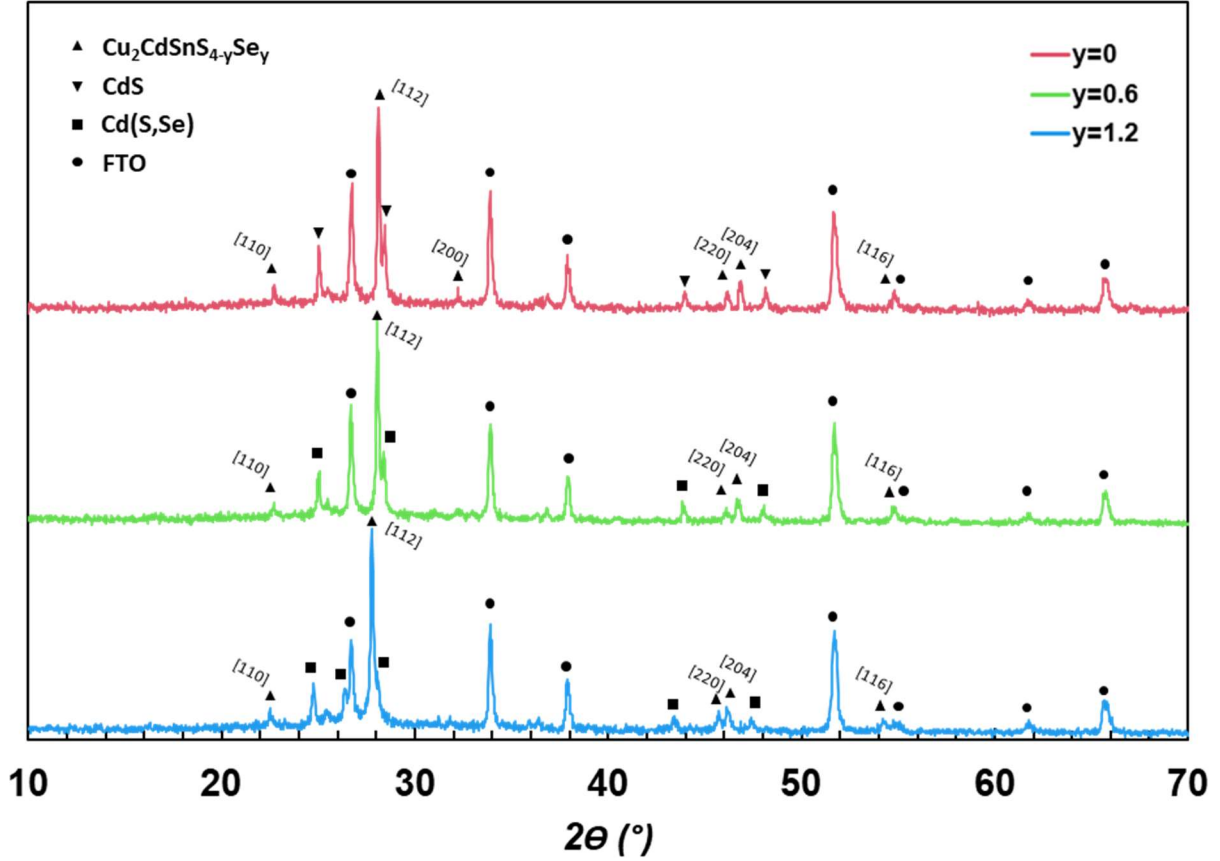


Figure 2. XRD spectra of the samples with different Se content, where the positions of the peaks corresponding to FTO, CdS, and CCTSSe are marked. The Miller indexes are indicated for the peaks corresponding to $\text{Cu}_2\text{CdSnS}_{4-y}\text{Se}_y$.

To elucidate the different phases present in the CCTSSe, we carried out Raman scattering spectra measurements from both sides: the front FTO contact side (**Figure 3a**) and the back side (**Figure 3b**). Raman spectra measured from front contact show a significant difference between the samples. The $y = 0$ sample shows mainly the presence of the $\text{Cu}_2\text{CdSnS}_4$ phase with the typical peaks at 284 and 332 cm^{-1} .⁴⁶ A small peak related to the CdS phase was observed at 305 cm^{-1} ,⁴⁷ and a peak at 143 cm^{-1} can be assigned to the TiO_2 phase.⁴⁸ Here, the relatively small intensity of the CdS peak can be explained by the slightly higher effective band gap as it was assessed from optical analysis, which results in exceeding the excitation laser energy by the bandgap energy. A band in the high wavenumbers range ($>500\text{ cm}^{-1}$) is attributed to the glass signal through which the Raman spectra of the front side were measured. Adding selenium in the sulfo-selenization treatment process results in a significant change of phase. In the case of the $y = 0.6$ sample, only peaks of Cd(S,Se) solid solution phase can be noted from the spectra. These include the first-order LO-like peaks at 194 and 299 cm^{-1} , and the second-order peaks at 398 , 492 , and 598 cm^{-1} . Here the position of the Raman peaks correlates with the presence of

Se in the ETL layer,⁴⁹ is in agreement with the X-ray analysis. The high intensity of the main Cd(S,Se) peaks is related to the proximity with the resonant conditions since the excitation wavelength is closer to the bandgap of the compound. In the Raman spectra measured in the $y = 1.2$ sample, a small displacement of the peaks compared to the $y = 0.6$ sample can be observed, mainly in the 194, 299, and 598 cm^{-1} peaks, in accordance with the increase of the Se content in the ETL layer.

The shift of the main peak of CCTSSe peaks to the lower wavenumber also correlates with the expected selenization of the absorber.

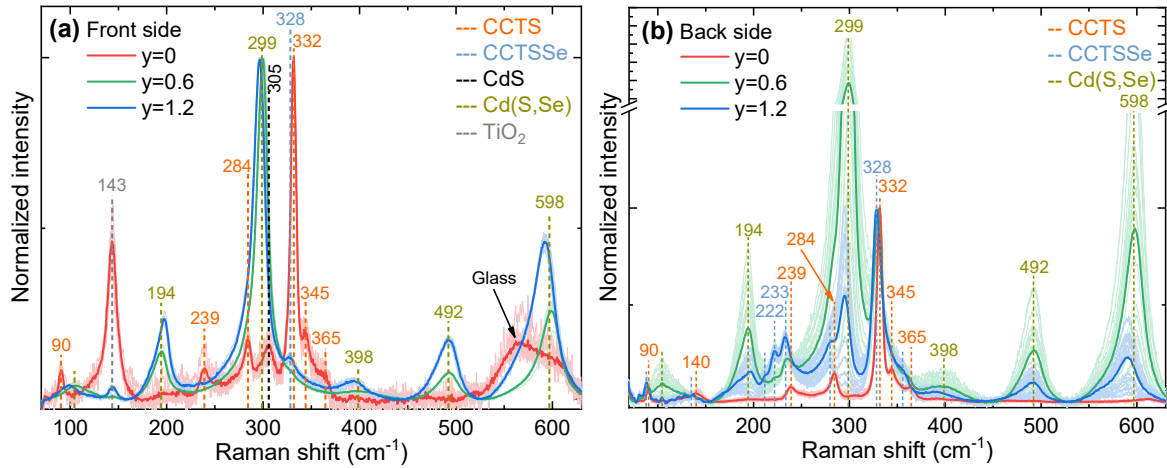


Figure 3. Raman scattering spectra of the CCTSSe absorbers measured from the side of (a) front and (b) back contact. Here the pale lines (resulting in a pale diffused spectral cloud) represent the individual spectra measured in different sample points and legible solid lines are the average of all spectra. The vertical dashed lines indicate the position of the Raman peaks, and their color corresponds to the different phases. Numbers indicate the position of the most intense Raman peaks in different phases.

The Raman spectra measured from the side of back contact (**Figure 3b**) in all samples show the presence of mainly similar phases as from the front side (detailed in **Figure S1b**). Here the, $y = 0$ sample shows only the peaks of the CCTS phase (at 90, 140, 239, 284, 332, 345, and 365 cm^{-1}). On the other hand, in the spectra of $y = 0.6$ and $y = 1.2$ samples, strong peaks of the Cd(S,Se) phase still appear. This can be related to the presence of pinholes in these samples, and the significant change in the intensity of these peaks from point to point is explained by the non-homogeneous distribution of the pinholes and/or their size. Nevertheless, the main peaks of the CCTSSe phase in the $y = 0.6$ and $y = 1.2$ samples become more pronounced, and the main peak of this phase can be seen at 330 and 328 cm^{-1} , respectively, correlating with the increased amount of Se in the absorber. This is also supported by the change of relative intensity of the

peaks close to 222 and 233 cm^{-1} (higher intensity in the $y = 1.2$ sample denotes higher Se content compared to the $y = 0.6$ sample), which can be assigned to the S-Se vibrations based on the study made in familiar $\text{Cu}_2\text{ZnSn}(\text{S},\text{Se})_4$ solid solution.⁵⁰ Finally, to assess the possible difference in the Se content in the $\text{Cd}(\text{S},\text{Se})$ phase, the average Raman spectra from different sides were compared (**Figure S1b**). A small shift of the peaks between the spectra measured from the front and back side has been observed. Taking into account that spectra measured from the front side collect the information from the whole depth of the ETL layer, the backside signal mainly comes from the interface (CdS/CCTSSe), and a small difference in the Se content is expected in-depth of the ETL layer.

Transmittance spectroscopy (**Figure 4a**) was used to note the impact on the transmittance to substrates before the deposition of the CCTS layer. The transmittance of the substrate is $\sim 75\%$ in the wavelengths above the bandgap of CdS, which is calculated to be 2.39 eV. **Figure 4b**, depicts the effect of the different annealing processes. A first decrease of the transmittance in the region of 900 nm is associated with the decrease of band-gap absorption of the light absorber, as estimated by the Tauc plot (**Figure S2a**), and presented in **Table 2**. Expectedly, a decrease of the band gap with the increasing content of selenium is noted, but in all cases maintains its suitability for photovoltaic applications. A second decrease is observed in the region of 500 nm, which can be associated with the change of the bandgap of the ETL modified by the annealing condition. The optical band gap (**Figure S2b**), is presented in **Table 2**. To note here the ETL band gap for the sample $y = 0$ was found to be slightly lower than for the as-deposited CdS. This difference can be due to the changes in the crystalline quality and/or possible doping by Cu or Sn atoms coming from the absorber to the CdS during the absorber synthesis.

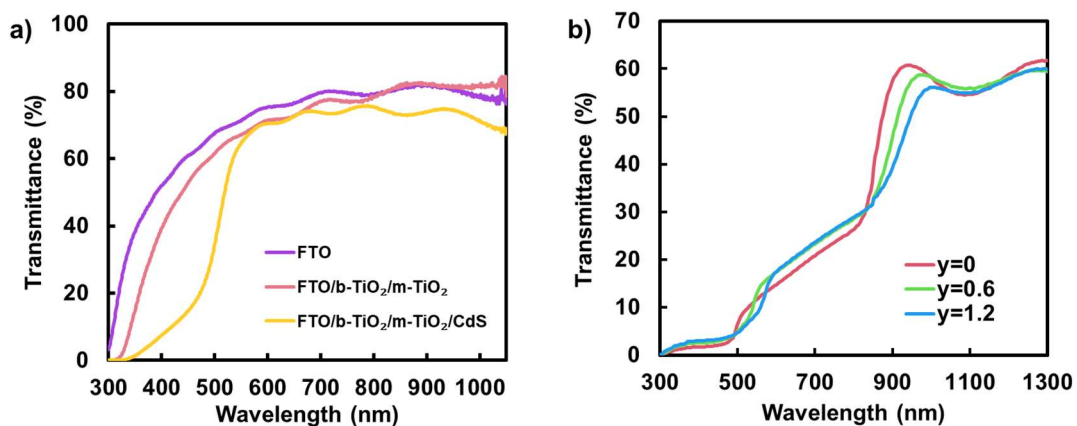


Figure 4. a) Transmittance spectra of the substrate after depositing each layer, and b) of the solar cells with different Se content.

For $y = 0.6$ and $y = 1.2$, a more drastic decrease in the ETL bandgap is noted. This decrease supports the change of composition of this layer during the sulfo-selenization treatment to a selenium Cd(S,Se) layer, as observed in XRD. The change of the band gap with the composition obeys Vegard's law for a Cd(S,Se) solid solution,⁵¹ and is following the hypothesis of having a homogeneous composition with the absorber.

Table 2. Optical and crystallographic properties of the $\text{Cu}_2\text{CdSn}(\text{S}_{4-y}\text{Se}_y)$ layer and $\text{Cd}(\text{S}_{1-x}\text{Se}_x)$ present in the samples. Standard errors are below 1 % for the E_g and below 0.1 % for the lattice parameters.

Sample	Composition	E_g (eV)	a (Å)	c (Å)	Cell Volume (Å ³)
$y = 0$	CdS	2.34	4.100	6.665	97.0
	$\text{Cu}_2\text{CdSnS}_4$	1.40	5.557	10.733	331.4
$y = 0.6$	$\text{Cd}(\text{S}_{0.85}\text{Se}_{0.15})$	2.10	4.105	6.670	97.3
	$\text{Cu}_2\text{CdSn}(\text{S}_{3.4}\text{Se}_{0.6})$	1.31	5.561	10.780	333.4
$y = 1.2$	$\text{Cd}(\text{S}_{0.7}\text{Se}_{0.3})$	2.00	4.149	6.751	100.7
	$\text{Cu}_2\text{CdSn}(\text{S}_{2.8}\text{Se}_{1.2})$	1.25	5.608	10.929	343.7

3.2 Optoelectronic characterization of complete cells

The PV parameters of the fabricated solar cells with the different conditions are presented (**Figure S3**) and the best devices along with statistics are tabulated (**Table 3**). The open-circuit voltage (V_{oc}) is higher in pure sulfur devices, which corresponds to its higher bandgap. Considering different bandgaps of the absorbers, the loss of V_{oc} compared with the ideal value remains nearly the same for the $y = 0$ and $y = 0.6$, but it is reduced in the $y = 1.2$ cases, suggesting that the inclusion of Se mitigates the recombination effects that affect the voltage. Similarly, a small increase in the current can be associated with a higher light absorption in the IR region as the band gap decrease.

The most affected parameter is the FF, with a significant increase for higher Se content, increasing from 27.5 % to 43.6 % on average. As shown in the J - V curves under illumination (**Figure 5a**), the shape of the curve has evolved, closer to a more ideal behavior for the samples

with higher Se. We associate this improvement with a longer charge carrier diffusion in the absorber layer.

Table 3. PV parameters of the best cell of each condition, and the averages over 12 or more cells under brackets.

Device	V_{OC} (mV)	J_{SC} (mA/cm ²)	FF (%)	PCE (%)	V_{OC} loss (mV)
y = 0	520 (501 ± 38)	16.15 (12.10 ± 2.6)	26.3 (27.5 ± 1.1)	2.21 (1.64 ± 0.32)	(629 ± 38)
y = 0.6	455 (441 ± 34)	14.09 (13.60 ± 1.3)	39.9 (33.6 ± 3.0)	2.55 (2.01 ± 0.27)	(629 ± 34)
y = 1.2	477 (442 ± 32)	16.86 (15.56 ± 2.0)	43.6 (40.4 ± 3.4)	3.50 (2.81 ± 0.59)	(568 ± 32)

The EQE measured (**Figure 5b**), depicts several effects on comparing the different conditions. First, there is an increase in the signal at shorter wavelengths, while the peak of efficiency shifts progressively to longer wavelengths with the increase of the Se ratio. The peak depends on the balance of light reaching the absorber and light absorbed by the ETL layer. Since the Se ratio reduces the band gap of the ETL, it can absorb light on a longer wavelength, thus shifting EQE spectra. A higher absorption is noted at longer wavelengths with the increase of Se content, associated with the reduction of the absorber band gap. The band edge is used to calculate the band gaps, obtaining values of 1.420, 1.356, and 1.285 eV for the samples y = 0, y = 0.6, and y = 1.2 respectively, which are coherent with the values measured by the Tauc plots previously.

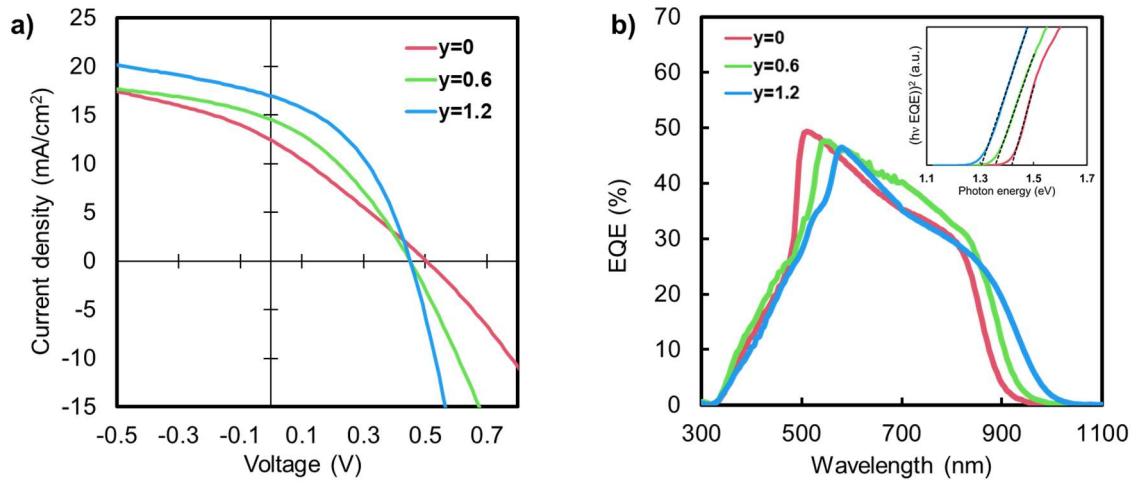


Figure 5. a) J - V curves of a device with the different conditions under 1 Sun illumination and b) EQE graph. The inset shows the band gap calculation from the band edge.

We derived the electronic parameters of the solar cells under dark conditions from the dark J - V curves (**Figure 6a**), a change in the turn-on voltage can be noticed, which correlates with the difference in the band gap of the absorber composition, affecting the diode properties of the solar cells. From the natural logarithm of the dark J - V curves (**Figure S4**), the diode factor n ,

dark saturation current J_0 , and series resistance R_s have been extracted, while the built-in potential (V_{BI}) is extracted from the C - V curves, and depletion width W_0 and carrier density N_D are calculated (**Figure 6b**) and presented in **Table 4** at $V = 0$. This parameter allows us to distinguish the fundamental differences between the composition and understand the keys for further improvements.

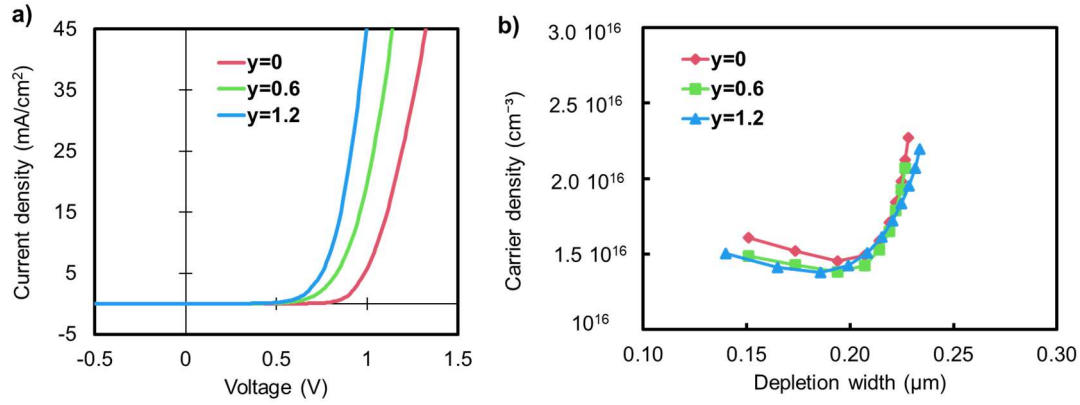


Figure 6. a) Dark J - V curve of the devices with different Se content and, b) carrier density and depletion width curve extracted from the capacitance-voltage (C - V) measurements.

Table 4. Electronic parameters extracted from dark J - V and C - V measurements.

Device	n	J_0 (A/cm²)	R_s (Ω cm²)	V_{BI} (V)	W_0 (μ m)	N_D (cm⁻³)
y = 0	2.29	2.9×10^{-10}	5.12	0.604	0.194	1.46×10^{16}
y = 0.6	2.87	8.1×10^{-8}	3.55	0.574	0.194	1.38×10^{16}
y = 1.2	2.80	1.5×10^{-7}	2.27	0.524	0.186	1.38×10^{16}

The $\text{Cu}_2\text{CdSn}(\text{S},\text{Se})_4$ characteristics obtained can be correlated with an array of optoelectronic properties. The shift in the band gap impacts the absorbed wavelengths, and therefore the J_{sc} . The band gap is reduced with the increase of selenium in the composition, leading to increase absorption in the infrared region but losing part of the UV region due to a parasitic absorption of the ETL. The change of ETL to a more transparent material can avoid this effect and will rationalize the $\text{Cu}_2\text{CdSn}(\text{S},\text{Se})_4$. The parallel reduction of the V_{oc} is also correlated with the change of the band gap energy, due to the thermalization of electron-hole pairs.

The series resistance acquires a significant reduction for the solar cells with higher Se content, which is a key factor for the improvement of the FF. The improvement of the resistance is prominent in the illuminated J - V curves, implying that the main improvement of resistance is in the hole diffusion in the absorber layer. The difference in the J_0 can be directly related to the

difference in the V_{BI} , which results from a shallowing of the Fermi level in the Se-containing absorbers. The V_{BI} also sets the practical limit for the V_{oc} . The difference between V_{BI} and V_{oc} is smaller in the $y = 1.2$ sample, which indicates a reduction of the interface recombination. Strategies of further increasing the V_{BI} , could result in a further increase of the V_{oc} . In all the solar cells, the calculated ideality factor (n) is higher than 2. A value close to 2 indicates that the recombination in the junction dominates, which is common in thin film-based solar cells, while the values above suggest an increase in the bulk trap density, due to recombination in the grain boundaries.⁵² Remarkably, the sample $y = 0$ has the lowest n value, and also presents fewer voids in the surface, thus ensuring the higher compactness of the layer and less bulk recombination. Strategies for passivation of the grain boundaries, increment in the grain size, and reducing the voids can produce a better diode quality and reduce the V_{oc} deficit.

The depletion width and carrier density are similar in all the samples, with values close to the solar cells reported on other kesterite compounds.^{3,53} A depletion width in the order of 200 nm implies that the absorber is mostly depleted, reducing the problem of collecting the photogenerated charges if they have a diffusion length within the order of the thickness of the absorber layer. The losses of current found in the longer wavelengths of the EQE can be ascribed to an insufficient diffusion length of the photogenerated electron-hole pairs, setting the electron diffusion length as the main limiting factor of the J_{sc} .

It is worth noting that the influence of the heterointerfaces properties, such as the band alignments, lattice match, or interface states impact the device performance and optoelectronic properties. A significant variation of the bands energy levels of CCTS in comparison with CZTS has been measured.⁵⁴ A rational band alignment between the films can facilitate charge extraction, so further studies focused on the absorber interfaces are required to push the performance of this promising photovoltaic technology.

We have elucidated that the inclusion of Se into the composition of the absorber mitigates the harmful processes that reduce the FF in superstrate solar cells. Superstrate solar cells using an absorber with a $\text{Cu}_2\text{CdSn}(\text{S}_{2.8}\text{Se}_{1.2})$ composition, prepared by spray pyrolysis from a water-ethanol-based solution, measures a PCE of 3.5 %, which is on par with the reports using similar absorber compositions in a substrate architecture⁴¹ moreover, with the best solution-process solar cells in superstrate architecture using environmentally friendly solvents.

4. Conclusions

We show that the introduction of Se in a $\text{Cu}_2\text{CdSnS}_4$ composition allows the control of the band gap while improving the required properties for their use as a light harvester. Higher content of Se improves the FF owing to a reduction in the series resistance while presenting a lower V_{oc}

deficit. The FF is almost doubled with the introduction of a 30 % of Se/(S+Se) relative content, which allows measuring a power conversion efficiency of 3.5 %, a state-of-the-art value reported for quaternary materials in a superstrate architecture, and comparable to similar materials used in a substrate architecture. However, a low electron diffusion length is a suspect of limiting the J_{SC} that affects the cells based both on $\text{Cu}_2\text{CdSnS}_4$ and $\text{Cu}_2\text{CdSn}(\text{S},\text{Se})_4$. Improving the crystalline quality could promote this type of solar cell as a green and cost-effective alternative to the current PV technologies and, simultaneously, avoid the use of critical or scarce elements.

Supporting information

Diffraction patterns and Raman spectra. Tauc-plot with bandgap estimations. Boxplots of solar cells characteristic parameters. Dark J - V curves at logarithmic scale.

Aknowlegments

This work has received funding from the European Union H2020 Programme under the European Research Council Consolidator grant [MOLEMAT, 726360]. Authors from IREC belong to the MNT-Solar Consolidated Research Group of the “Generalitat de Catalunya” (ref. 2021 SGR 01286) and are grateful to European Regional Development Funds (ERDF, FEDER Programa Competitivitat de Catalunya 2007–2013). MG acknowledges the financial support from the Spanish Ministry of Science, Innovation and Universities within the Juan de la Cierva fellowship (IJC2018-038199-I).

References

- (1) Wilson, G. M.; Al-Jassim, M.; Metzger, W. K.; Glunz, S. W.; Verlinden, P.; Xiong, G.; Mansfield, L. M.; Stanbery, B. J.; Zhu, K.; Yan, Y.; Berry, J. J.; Ptak, A. J.; Dimroth, F.; Kayes, B. M.; Tamboli, A. C.; Peibst, R.; Catchpole, K.; Reese, M. O.; Klinga, C. S.; Denholm, P.; Morjaria, M.; Deceglie, M. G.; Freeman, J. M.; Mikofski, M. A.; Jordan, D. C.; Tamizhmani, G.; Sulas-Kern, D. B. The 2020 Photovoltaic Technologies Roadmap. *Journal of Physics D: Applied Physics*. 2020. <https://doi.org/10.1088/1361-6463/ab9c6a>.
- (2) Gong, Y.; Zhang, Y.; Zhu, Q.; Zhou, Y.; Qiu, R.; Niu, C.; Yan, W.; Huang, W.; Xin, H. Identifying the Origin of the Voc Deficit of Kesterite Solar Cells from the Two Grain Growth Mechanisms Induced by Sn^{2+} and Sn^{4+} precursors in DMSO Solution. *Energy Environ Sci* **2021**, 14 (4), 2369–2380. <https://doi.org/10.1039/d0ee03702h>.

- (3) Wang, W.; Winkler, M. T.; Gunawan, O.; Gokmen, T.; Todorov, T. K.; Zhu, Y.; Mitzi, D. B. Device Characteristics of CZTSSe Thin-Film Solar Cells with 12.6% Efficiency. *Adv Energy Mater* **2014**, 4 (7), 1–5. <https://doi.org/10.1002/aenm.201301465>.
- (4) Colina, M.; Bailo, E.; Medina-Rodríguez, B.; Kondrotas, R.; Sánchez-González, Y.; Sylla, D.; Placidi, M.; Blanes, M.; Ramos, F.; Cirera, A.; Pérez Rodríguez, A.; Saucedo, E. Optimization of Ink-Jet Printed Precursors for Cu₂ZnSn(S,Se)₄solar Cells. *J Alloys Compd* **2018**, 735, 2462–2470. <https://doi.org/10.1016/j.jallcom.2017.12.035>.
- (5) Larramona, G.; Levchenko, S.; Bourdais, S.; Jacob, A.; Choné, C.; Delatouche, B.; Moisan, C.; Just, J.; Unold, T.; Dennler, G. Fine-Tuning the Sn Content in CZTSSe Thin Films to Achieve 10.8% Solar Cell Efficiency from Spray-Deposited Water-Ethanol-Based Colloidal Inks. *Adv Energy Mater* **2015**, 5 (24), 1–10. <https://doi.org/10.1002/aenm.201501404>.
- (6) Enkhbat, T.; Kim, S.; Kim, J. Device Characteristics of Band Gap Tailored 10.04% Efficient CZTSSe Solar Cells Sprayed from Water-Based Solution. *ACS Appl Mater Interfaces* **2019**, 11 (40), 36735–36741. <https://doi.org/10.1021/acsami.9b12565>.
- (7) Nakayama, N.; Ito, K. Sprayed Films of Stannite Cu₂ZnSnS₄. *Appl Surf Sci* **1996**, 92, 171–175.
- (8) Grinciene, G.; Franckevičius, M.; Kondrotas, R.; Giraitis, R.; Juškenas, R.; Niaura, G.; Naujokaitis, A.; Juodkazyte, J.; TamašauskaiteTamašiūnaitė, L.; Pakštas, V. Spray Pyrolysis Approach to CZTSSe Thin Films. Influence of Solvents on Film Characteristics. *Semicond Sci Technol* **2018**, 33 (9), 095013. <https://doi.org/10.1088/1361-6641/AAD5D0>.
- (9) Payno, D.; Kazim, S.; Ahmad, S. Impact of Cation Substitution in All Solution-Processed Cu₂(Cd, Zn)SnS₄superstrate Solar Cells. *J Mater Chem C Mater* **2021**, 9 (48), 17392–17400. <https://doi.org/10.1039/d1tc04527j>.
- (10) Scragg, J. J. S.; Larsen, J. K.; Kumar, M.; Persson, C.; Sendler, J.; Siebentritt, S.; Platzer Björkman, C. Cu-Zn Disorder and Band Gap Fluctuations in Cu₂ZnSn(S,Se)₄: Theoretical and Experimental Investigations. *Phys Status Solidi B Basic Res* **2016**, 253 (2), 247–254. <https://doi.org/10.1002/pssb.201552530>.
- (11) Just, J.; Sutter-Fella, C. M.; Lützenkirchen-Hecht, D.; Frahm, R.; Schorr, S.; Unold, T. Secondary Phases and Their Influence on the Composition of the Kesterite Phase in CZTS and CZTSe Thin Films. *Physical Chemistry Chemical Physics* **2016**, 18 (23), 15988–15994. <https://doi.org/10.1039/c6cp00178e>.

- (12) Tsega, M.; Kuo, D.-H. H. Defects and Its Effects on Properties of Cu-Deficient Cu₂ZnSnSe₄ Bulks with Different Zn/Sn Ratios. *Applied Physics Express* **2012**, *5* (9), 091201. <https://doi.org/10.1143/APEX.5.091201>.
- (13) Lee, Y. S.; Gershon, T.; Gunawan, O.; Todorov, T. K.; Gokmen, T.; Virgus, Y.; Guha, S. Cu₂ZnSnSe₄ Thin-Film Solar Cells by Thermal Co-Evaporation with 11.6% Efficiency and Improved Minority Carrier Diffusion Length. *Adv Energy Mater* **2015**, *5* (7), 2–5. <https://doi.org/10.1002/aenm.201401372>.
- (14) Gokmen, T.; Gunawan, O.; Todorov, T. K.; Mitzi, D. B. Band Tailing and Efficiency Limitation in Kesterite Solar Cells. *Appl Phys Lett* **2013**, *103* (10), 103506. <https://doi.org/10.1063/1.4820250>.
- (15) Li, X.; Zhuang, D.; Zhang, N.; Zhao, M.; Yu, X.; Liu, P.; Wei, Y.; Ren, G. Achieving 11.95% Efficient Cu₂ZnSnSe₄ Solar Cells Fabricated by Sputtering a Cu-Zn-Sn-Se Quaternary Compound Target with a Selenization Process. *J Mater Chem A Mater* **2019**, *7* (16), 9948–9957. <https://doi.org/10.1039/c9ta00385a>.
- (16) Redinger, A.; Unold, T. High Surface Recombination Velocity Limits Quasi-Fermi Level Splitting in Kesterite Absorbers. *Sci Rep* **2018**, *8* (1), 1874. <https://doi.org/10.1038/s41598-018-19798-w>.
- (17) Antunez, P. D.; Bishop, D. M.; Luo, Y.; Haight, R. Efficient Kesterite Solar Cells with High Open-Circuit Voltage for Applications in Powering Distributed Devices. *Nat Energy* **2017**, *2* (11), 884–890. <https://doi.org/10.1038/s41560-017-0028-5>.
- (18) Chen, W.-C. C.; Chen, C. H. C.-Y. Y. C.-H.; Lin, Y.-R. R.; Chang, J.-K. K.; Chen, C. H. C.-Y. Y. C.-H.; Chiu, Y.-P. P.; Wu, C.-I. I.; Chen, K.-H. H.; Chen, L.-C. C. Interface Engineering of CdS/CZTSSe Heterojunctions for Enhancing the Cu₂ZnSn(S,Se)₄ Solar Cell Efficiency. *Mater Today Energy* **2019**, *13* (1), 256–266. <https://doi.org/10.1016/j.mtener.2019.05.015>.
- (19) Hwang, D. K.; Ko, B. S.; Jeon, D. H.; Kang, J. K.; Sung, S. J.; Yang, K. J.; Nam, D.; Cho, S.; Cheong, H.; Kim, D. H. Single-Step Sulfo-Selenization Method for Achieving Low Open Circuit Voltage Deficit with Band Gap Front-Graded Cu₂ZnSn(S,Se)₄ Thin Films. *Solar Energy Materials and Solar Cells* **2017**, *161* (November 2016), 162–169. <https://doi.org/10.1016/j.solmat.2016.11.034>.
- (20) Dimitrievska, M.; Giraldo, S.; Pistor, P.; Saucedo, E.; Pérez-Rodríguez, A.; Izquierdo-Roca, V. Raman Scattering Analysis of the Surface Chemistry of Kesterites: Impact of Post-Deposition Annealing and Cu/Zn Reordering on Solar Cell Performance. *Solar*

- Energy Materials and Solar Cells* **2016**, *157*, 462–467. <https://doi.org/10.1016/j.solmat.2016.07.009>.
- (21) Payno, D.; Kazim, S.; Salado, M.; Ahmad, S. Sulfurization Temperature Effects on Crystallization and Performance of Superstrate CZTS Solar Cells. *Solar Energy* **2021**, *224*, 1136–1143. <https://doi.org/10.1016/j.solener.2021.06.038>.
 - (22) Wang, Z.; Brodusch, N.; Gauvin, R.; Demopoulos, G. P. New Insight into Sulfurized and Selenized Kesterite-Titania Nanostructures for CdS-Free and HTM-Free Photovoltaic and Voltage-Modulated Photodetecting Applications. *ACS Sustain Chem Eng* **2019**, *7* (17), 15093–15101. <https://doi.org/10.1021/acssuschemeng.9b03814>.
 - (23) Wang, Z.; Brodusch, N.; Gauvin, R.; Demopoulos, G. P. Lithium-Doped Cu₂ZnSnS₄ Superstrate Solar Cells with 5% Efficiency – An Alternative to Thin Film Kesterite Photovoltaics. *Nano Energy* **2018**, *53* (August), 130–134. <https://doi.org/10.1016/j.nanoen.2018.08.049>.
 - (24) Franckevičius, M.; Pakštas, V.; Grincienė, G.; Kamarauskas, E.; Giraitis, R.; Nekrasovas, J.; Selskis, A.; Juškėnas, R.; Niaura, G. Efficiency Improvement of Superstrate CZTSSe Solar Cells Processed by Spray Pyrolysis Approach. *Solar Energy* **2019**, *185* (January), 283–289. <https://doi.org/10.1016/j.solener.2019.04.072>.
 - (25) Prabhakar, T.; Jampana, N. Effect of Sodium Diffusion on the Structural and Electrical Properties of Cu₂ZnSnS₄ Thin Films. *Solar Energy Materials and Solar Cells* **2011**, *95* (3), 1001–1004. <https://doi.org/10.1016/j.solmat.2010.12.012>.
 - (26) Xin, H.; Vorpahl, S. M.; Collord, A. D.; Braly, I. L.; Uhl, A. R.; Krueger, B. W.; Ginger, D. S.; Hillhouse, H. W. Lithium-Doping Inverts the Nanoscale Electric Field at the Grain Boundaries in Cu₂ZnSn(S,Se)₄ and Increases Photovoltaic Efficiency. *Physical Chemistry Chemical Physics* **2015**, *17* (37), 23859–23866. <https://doi.org/10.1039/c5cp04707b>.
 - (27) Zhou, J.; Xu, X.; Duan, B.; Wu, H.; Shi, J.; Luo, Y.; Li, D.; Meng, Q. Regulating Crystal Growth via Organic Lithium Salt Additive for Efficient Kesterite Solar Cells. *Nano Energy* **2021**, *89*, 106405. <https://doi.org/10.1016/j.nanoen.2021.106405>.
 - (28) Mule, A.; Vermang, B.; Sylvester, M.; Brammertz, G.; Ranjbar, S.; Schnabel, T.; Gampa, N.; Meuris, M.; Poortmans, J. Effect of Different Alkali (Li, Na, K, Rb, Cs) Metals on Cu₂ZnSnSe₄ Solar Cells. *Thin Solid Films* **2017**, *633*, 156–161. <https://doi.org/10.1016/j.tsf.2016.11.027>.

- (29) Wang, Z.; Wang, Y.; Taghipour, N.; Peng, L.; Konstantatos, G. Ag-Refined Kesterite in Superstrate Solar Cell Configuration with 9.7% Power Conversion Efficiency. *Adv Funct Mater* **2022**, 32 (43), 2205948. <https://doi.org/10.1002/adfm.202205948>.
- (30) Su, Z.; Tan, J. M. R.; Li, X.; Zeng, X.; Batabyal, S. K.; Wong, L. H. Cation Substitution of Solution-Processed Cu₂ZnSnS₄ Thin Film Solar Cell with over 9% Efficiency. *Adv Energy Mater* **2015**, 5 (19), 1500682. <https://doi.org/10.1002/aenm.201500682>.
- (31) Hadke, S.; Chen, W.; Tan, J. M. R.; Guc, M.; Izquierdo-Roca, V.; Rignanese, G. M.; Hautier, G.; Wong, L. H. Effect of Cd on Cation Redistribution and Order-Disorder Transition in Cu₂(Zn,Cd)SnS₄. *J Mater Chem A Mater* **2019**, 7 (47), 26927–26933. <https://doi.org/10.1039/c9ta09572a>.
- (32) Fan, P.; Lin, J.; Hu, J.; Yu, Z.; Zhao, Y.; Chen, S.; Zheng, Z.; Luo, J.; Liang, G.; Su, Z. Over 10% Efficient Cu₂CdSnS₄ Solar Cells Fabricated from Optimized Sulfurization. *Adv Funct Mater* **2022**, 2207470. <https://doi.org/10.1002/ADFM.202207470>.
- (33) Todorov, T. K.; Reuter, K. B.; Mitzi, D. B. High-Efficiency Solar Cell with Earth-Abundant Liquid-Processed Absorber. *Advanced Materials* **2010**, 22 (20), 156–159. <https://doi.org/10.1002/adma.200904155>.
- (34) Dimitrievska, M.; Fairbrother, A.; Gunder, R.; Gurieva, G.; Xie, H.; Saucedo, E.; Pérez-Rodríguez, A.; Izquierdo-Roca, V.; Schorr, S. Role of S and Se Atoms on the Microstructural Properties of Kesterite Cu₂ZnSn(S_xSe_{1-x})₄ Thin Film Solar Cells. *Physical Chemistry Chemical Physics* **2016**, 18 (12), 8692–8700. <https://doi.org/10.1039/C5CP07577G>.
- (35) Wei, Y.; Zhuang, D.; Zhao, M.; Gong, Q.; Sun, R.; Zhang, L.; Lyu, X.; Peng, X.; Ren, G.; Wu, Y.; Wei, J. Effects of Selenium Atmosphere on Grain Growth for CZTSe Absorbers Fabricated by Selenization of As-Sputtered Precursors. *J Alloys Compd* **2018**, 755, 224–230. <https://doi.org/10.1016/J.JALLCOM.2018.04.311>.
- (36) Temgoua, S.; Bodeux, R.; Naghavi, N. Influence of the Annealing Atmosphere and Precursor's Thickness on the Properties of CZTSSe Based Solar Cells. *Solar Energy Materials and Solar Cells* **2019**, 191, 123–132. <https://doi.org/10.1016/J.SOLMAT.2018.11.001>.
- (37) Matsushita, H.; Maeda, T.; Katsui, A.; Takizawa, T. Thermal Analysis and Synthesis from the Melts of Cu-Based Quaternary Compounds Cu–III–IV–VI₄ and Cu₂–II–IV–VI₄ (II=Zn, Cd; III=Ga, In; IV=Ge, Sn; VI=Se). *J Cryst Growth* **2000**, 208 (1–4), 416–422. [https://doi.org/10.1016/S0022-0248\(99\)00468-6](https://doi.org/10.1016/S0022-0248(99)00468-6).

- (38) Liu, M. L.; Chen, I. W.; Huang, F. Q.; Chen, L. D. Improved Thermoelectric Properties of Cu-Doped Quaternary Chalcogenides of $\text{Cu}_2\text{CdSnSe}_4$. *Advanced Materials* **2009**, *21* (37), 3808–3812. <https://doi.org/10.1002/adma.200900409>.
- (39) Fan, F. J.; Yu, B.; Wang, Y. X.; Zhu, Y. L.; Liu, X. J.; Yu, S. H.; Ren, Z. Colloidal Synthesis of $\text{Cu}_2\text{CdSnSe}_4$ Nanocrystals and Hot-Pressing to Enhance the Thermoelectric Figure-of-Merit. *J Am Chem Soc* **2011**, *133* (40), 15910–15913. <https://doi.org/10.1021/ja207159j>.
- (40) Ibáñez, M.; Cadavid, D.; Zamani, R.; García-Castelló, N.; Izquierdo-Roca, V.; Li, W.; Fairbrother, A.; Prades, J. D.; Shavel, A.; Arbiol, J.; Pérez-Rodríguez, A.; Morante, J. R.; Cabot, A. Composition Control and Thermoelectric Properties of Quaternary Chalcogenide Nanocrystals: The Case of Stannite $\text{Cu}_2\text{CdSnSe}_4$. *Chemistry of Materials* **2012**, *24* (3), 562–570. <https://doi.org/10.1021/CM2031812>.
- (41) Zhao, W.; Wang, G.; Tian, Q.; Huang, L.; Gao, S.; Pan, D. Solution-Processed $\text{Cu}_2\text{CdSn}(\text{S},\text{Se})_4$ Thin Film Solar Cells. *Solar Energy Materials and Solar Cells* **2015**, *133*, 15–20. <https://doi.org/10.1016/J.SOLMAT.2014.10.040>.
- (42) Fthenakis, V. M. *Life Cycle Impact Analysis of Cadmium in CdTe PV Production*; Pergamon, 2004; Vol. 8. <https://doi.org/10.1016/j.rser.2003.12.001>.
- (43) Kumar, M.; Dubey, A.; Adhikari, N.; Venkatesan, S.; Qiao, Q. Strategic Review of Secondary Phases, Defects and Defect-Complexes in Kesterite CZTS-Se Solar Cells. *Energy Environ Sci* **2015**, *8* (11), 3134–3159. <https://doi.org/10.1039/c5ee02153g>.
- (44) Zhang, Q.; Deng, H.; Chen, L.; Tao, J.; Yu, J.; Yang, P.; Chu, J. Effects of Sulfurization Temperature on the Structural and Optical Properties of $\text{Cu}_2\text{CdSnS}_4$ Thin Films Prepared by Direct Liquid Method. *Mater Lett* **2017**, *193*, 206–209. <https://doi.org/10.1016/J.MATLET.2017.02.002>.
- (45) Fan, P.; Lin, J.; Hu, J.; Yu, Z.; Zhao, Y.; Chen, S.; Zheng, Z.; Luo, J.; Liang, G.; Su, Z. Over 10% Efficient $\text{Cu}_2\text{CdSnS}_4$ Solar Cells Fabricated from Optimized Sulfurization. *Adv Funct Mater* **2022**, 2207470. <https://doi.org/10.1002/ADFM.202207470>.
- (46) Pilvet, M.; Kauk-Kuusik, M.; Altosaar, M.; Grossberg, M.; Danilson, M.; Timmo, K.; Mere, A.; Mikli, V. Compositionally Tunable Structure and Optical Properties of $\text{Cu}_{1.85}(\text{Cd}_x\text{Zn}_{1-x})_{1.1}\text{SnS}_4$ ($0 \leq x \leq 1$) Monograin Powders. *Thin Solid Films* **2015**, *582*, 180–183. <https://doi.org/10.1016/j.tsf.2014.10.091>.
- (47) Atlan, F.; Becerril-Romero, I.; Giraldo, S.; Rotaru, V.; Sánchez, Y.; Gurieva, G.; Schorr, S.; Arushanov, E.; Pérez-Rodríguez, A.; Izquierdo-Roca, V.; Guc, M. Stability of $\text{Cu}_2\text{ZnSnSe}_4/\text{CdS}$ Heterojunction Based Solar Cells under Soft Post-Deposition Thermal

- Treatments. *Solar Energy Materials and Solar Cells* **2023**, *249*, 112046. <https://doi.org/10.1016/j.solmat.2022.112046>.
- (48) Golubović, A.; Šćepanović, M.; Kremenović, A.; Aškračić, S.; Berec, V.; Dohčević-Mitrović, Z.; Popović, Z. v. Raman Study of the Variation in Anatase Structure of TiO₂ Nanopowders Due to the Changes of Sol-Gel Synthesis Conditions. *J Solgel Sci Technol* **2009**, *49* (3), 311–319. <https://doi.org/10.1007/s10971-008-1872-3>.
- (49) Bischof, T.; Ivanda, M.; Lermann, G.; Materny, A.; Kiefer, W.; Kalus, J. Linear and Nonlinear Raman Studies on CdS_xSe_{1-x} - X Doped Glasses. *Journal of Raman Spectroscopy* **1996**, *27* (3–4), 297–302. [https://doi.org/10.1002/\(sici\)1097-4555\(199603\)27:3/4<297::aid-jrs964>3.0.co;2-j](https://doi.org/10.1002/(sici)1097-4555(199603)27:3/4<297::aid-jrs964>3.0.co;2-j).
- (50) Dimitrievska, M.; Xie, H.; Fairbrother, A.; Fontané, X.; Gurieva, G.; Saucedo, E.; Pérez-Rodríguez, A.; Schorr, S.; Izquierdo-Roca, V. Multiwavelength Excitation Raman Scattering of Cu₂ZnSn(S_xSe_{1-x})₄ (0 ≤ x ≤ 1) Polycrystalline Thin Films: Vibrational Properties of Sulfoselenide Solid Solutions. *Appl Phys Lett* **2014**, *105* (3), 031913. <https://doi.org/10.1063/1.4891333>.
- (51) Shahane, G. S.; More, B. M.; Rotti, C. B.; Deshmukh, L. P. Studies on Chemically Deposited CdS_{1-x}Se_x Mixed Thin Films. *Mater Chem Phys* **1997**, *47* (2–3), 263–267. [https://doi.org/10.1016/S0254-0584\(97\)80062-4](https://doi.org/10.1016/S0254-0584(97)80062-4).
- (52) Sozzi, G.; Mosca, R.; Calicchio, M.; Menozzi, R. Anomalous Dark Current Ideality Factor (n > 2) in Thin-Film Solar Cells: The Role of Grain-Boundary Defects. In *2014 IEEE 40th Photovoltaic Specialist Conference, PVSC 2014*; Institute of Electrical and Electronics Engineers Inc., 2014; pp 1718–1721. <https://doi.org/10.1109/PVSC.2014.6925252>.
- (53) Payno, D.; Sánchez, Y.; Blázquez, O.; Giraldo, S.; Salado, M.; Kazim, S.; Saucedo, E.; Ahmad, S. Partial Substitution of the CdS Buffer Layer with Interplay of Fullerenes in Kesterite Solar Cells. *J Mater Chem C Mater* **2020**, *8* (36), 12533–12542. <https://doi.org/10.1039/d0tc02666b>.
- (54) Rondiya, S. R.; Jadhav, Y.; Dzade, N. Y.; Ahammed, R.; Goswami, T.; De Sarkar, A.; Jadkar, S.; Haram, S.; Ghosh, H. N. Experimental and Theoretical Study into Interface Structure and Band Alignment of the Cu₂Zn_{1-x}Cd_xSnS₄ Heterointerface for Photovoltaic Applications. *ACS Appl Energy Mater* **2020**, *3* (6), 5153–5162. https://doi.org/10.1021/ACSAEM.9B02314/ASSET/IMAGES/LARGE/AE9B02314_0006.JPEG.